

Anomalous electronic and thermoelectric transport properties in cubic Rb₃AuO antiperovskiteYinchang Zhao^{1,*}, Chao Lian^{2,3}, Shuming Zeng^{4,5}, Zhenhong Dai^{1,†}, Sheng Meng^{3,6,‡} and Jun Ni^{4,5,§}¹Department of Physics, Yantai University, Yantai 264005, China²Oden Institute and Department of Physics, The University of Texas at Austin, Austin, Texas 78712, USA³Institute of Physics, Chinese Academy of Sciences, Beijing 100190, China⁴Department of Physics, Tsinghua University, Beijing 100084, China⁵Frontier Science Center for Quantum Information, Beijing 100084, China⁶Collaborative Innovation Center of Quantum Matter, Beijing 100871, China

(Received 23 May 2020; revised 10 September 2020; accepted 14 September 2020; published 28 September 2020)

We use first-principles calculations combined with self-consistent phonon (SCP) theory, electron-phonon (e - ph) coupling, and the Boltzmann transport equation (BTE) to investigate the electronic and thermoelectric transport properties in the cubic Rb₃AuO antiperovskite with strongly cubic and quartic lattice anharmonicity. The combination of SCP theory and Wannier-Fourier interpolation is used to calculate the e - ph coupling due to the failure of density functional perturbation theory in solving e - ph matrix elements for a strongly anharmonic crystal. Our results exhibit that a high electron mobility μ_e , e.g., ~ 454 cm²/Vs at 300 K from the iterative BTE solution, and a relatively weak temperature dependence of $\mu_e \propto T^{-1.1}$ are obtained in the n -type cubic Rb₃AuO. We demonstrate that the coupling between electrons and polar optical phonons is responsible for the good charge transport, which, along with the high thermopower deriving from a light and threefold degenerate conduction-band pocket around the X point, leads to a very high power factor reaching 5.5 mW/mK² at 800 K. Meanwhile, a low lattice thermal conductivity and an undersized Lorenz number that signifies a resulting low electron thermal conductivity are also detected. As a result, a good thermoelectric performance with a figure of merit $ZT \sim 1.02$ at 300 K and an anomalously high $ZT \sim 3.02$ at 800 K is captured in the n -type cubic Rb₃AuO. This finding breaks the long-term record of $ZT < 3$ in most of the reported bulk thermoelectric materials to date, and illustrates that the cubic Rb₃AuO is an excellent candidate for thermoelectric applications.

DOI: [10.1103/PhysRevB.102.094314](https://doi.org/10.1103/PhysRevB.102.094314)**I. INTRODUCTION**

Thermoelectric (TE) materials have attracted great attention due to their ability for direct conversion of electricity from heat [1–4]. The conversion efficiency is determined by the dimensionless figure of merit $ZT = S^2\sigma T/(\kappa_e + \kappa_l)$, where S , σ , T , and κ_e (κ_l) are the thermopower, electrical conductivity, absolute temperature, and electron (lattice) thermal conductivity, respectively. Hence, the optimization of ZT refers to the tuning of conflicting material properties through reducing the total thermal conductivity (κ_e and κ_l) and enhancing the TE power factor $S^2\sigma$ simultaneously. The former involves nanostructuring [5], substructuring [6,7], complexity [8,9], anharmonicity [10], and ferroelectriclike lattice instability [11,12], while the latter is usually achieved by band tuning [13], heavy doping [2,14], and the carrier energy filtering effect [15]. Generally, decreasing thermal conductivity is not hard since the κ_l can even be reduced to the lower limit of amorphous [16–27]. In contrast, the tuning of the power factor suffers from the counteractive behavior of S and σ with re-

spect to the change of carrier concentration. Therefore, to gain a high power factor, the electronic bands with anisotropic features, e.g., the coexistence of flat and dispersive band edges, have been proposed [28–30], where the flat part induces high S , while the dispersive part facilitates high carrier mobility.

Although there are many strategies to enhance TE conversion efficiency, most of the reported TE materials to date have the ZT values below 2, and only a few cases have the conversion efficiencies surpassing $ZT = 2$, such as cubic AgPb_{*m*}SbTe_{2+*m*} with a $ZT \sim 2.2$ [31], Ge_{1-*x*}Sb_{*x*}In_{*y*}Te with a $ZT \sim 2.3$ [32], and SnSe crystal with a highest $ZT \sim 2.6$ [11]. Recently, a remarkably high $ZT \sim 5$ has been predicted in the n -type Ba₂BiAu full-Heusler compound due to the coexistence of ultralow lattice thermal conductivity and an ultrahigh power factor [33], breaking the long-term record of $ZT < 3$. However, the Ba₂BiAu compound has not been synthesized, which poses a new challenge for achieving high TE conversion efficiency. In this work, enlightened by low lattice thermal conductivity [34] and an available experimental preparation scheme [35,36], we turn to the Rb₃AuO antiperovskite to search for the feasible high- ZT material.

Concretely, the stable Rb₃AuO crystal adopts the ideal cubic antiperovskite structure with the symmetric group of $Pm\bar{3}m$ and the fusing point of 850 K [37]. It can be prepared experimentally according to the procedure provided by Feldmann [35,36], and the anionic character of its gold atom has

*y.zhao@ytu.edu.cn

†zhdai@ytu.edu.cn

‡smeng@iphy.ac.cn

§junni@mail.tsinghua.edu.cn

been established by the x-ray absorption spectroscopy [38]. Theoretically, first-principles calculations have predicted that the cubic Rb_3AuO crystal is a semiconductor with strongly cubic and quartic lattice anharmonicity [34,39]. Therefore, a fairly low lattice thermal conductivity κ_l , e.g., ~ 0.7 W/mK at 300 K, with an anomalously weak temperature dependence of $\kappa_l \propto T^{-3}$, has been obtained in the cubic Rb_3AuO [34]. Obviously, if there is a high electrical conductivity σ , a phonon-glass electron-crystal characteristic will be captured in this material, which is usually required for a promising TE candidate.

In this paper, to gain the electronic transport and TE properties, we use the Boltzmann transport equation (BTE) combined with electron-phonon (*e-ph*) coupling to calculate the mobility μ , electrical conductivity σ , thermopower S , and electron thermal conductivity κ_e in the cubic Rb_3AuO with strong lattice anharmonicity. Due to the failure of density functional perturbation theory (DFPT) [40] to solve *e-ph* matrix elements for a strongly anharmonic crystal [41,42], we introduce self-consistent phonon (SCP) theory [43–48] along with Wannier-Fourier interpolation [49–54] to calculate the *e-ph* coupling. Our key findings are that the coexistence of high electron mobility dominated by the *e-ph* scattering on polar optical phonons and high thermopower deriving from the light and threefold degenerate conduction-band pocket gives rise to a high power factor, which, coupled with low κ_l and the undersized Lorenz number that signifies low κ_e , results in a good TE performance, with a highest $ZT > 1$ at 300 K and an anomalously high $ZT > 3$ at 800 K in the *n*-type cubic Rb_3AuO crystal.

II. METHODOLOGY

The involved first-principles calculations are carried out within the generalized gradient approximation (GGA) of the PBESOL functional [55] to the density functional theory (DFT) with plane waves simulating the valence electrons and norm-conserving pseudopotentials [56] describing the ion cores, as implemented in the QUANTUM ESPRESSO package [57]. The cutoff for plane-wave kinetic energy and charge density is set to be 90 and 360 Ry, respectively, in structure optimization and calculations for energy forces to fit the interatomic force constants (IFCs). For computing the *e-ph* scattering, the key quantities are the *e-ph* matrix elements,

$$g_{mnv}(\mathbf{k}, \mathbf{q}) = \sqrt{\frac{\hbar}{2\omega'_{\mathbf{q}v}}} \sum_{s\alpha} \frac{\mathbf{e}'_{\mathbf{q}vs\alpha}}{\sqrt{M_s}} \langle m\mathbf{k} + \mathbf{q} | \partial_{\mathbf{q}s\alpha} V | n\mathbf{k} \rangle, \quad (1)$$

which represent the probability amplitude of scattering induced by phonon mode $|\mathbf{q}v\rangle$ (with wave vector \mathbf{q} , mode index v , energy $\hbar\omega'_{\mathbf{q}v}$, and eigenvector $\mathbf{e}'_{\mathbf{q}v}$) between the Bloch states $|n\mathbf{k}\rangle$ and $|m\mathbf{k} + \mathbf{q}\rangle$ with band index n and crystal momentum \mathbf{k} . Here, $\partial_{\mathbf{q}s\alpha} V \equiv \sum_l e^{i\mathbf{q}\cdot\mathbf{R}_l} \partial_{l s\alpha} V$, and $\partial_{l s\alpha} V$ is the derivative of the Kohn-Sham potential with respect to displacement of atom s (with mass M_s) in the unit cell \mathbf{R}_l along the Cartesian direction α . To include the lattice anharmonic effect, the anharmonicity-renormalized frequencies $\omega'_{\mathbf{q}v}$ and eigenvectors $\mathbf{e}'_{\mathbf{q}v}$ at each considered temperature are adopted in Eq. (1) instead of the harmonic frequencies $\omega_{\mathbf{q}v}$ and eigenvectors $\mathbf{e}_{\mathbf{q}v}$ obtained from DFPT results. The SCP theory

coded in the ALAMODE package [44,45] is used to calculate the temperature-dependent anharmonicity, and the needed second- to fourth-order IFCs are trained by the compressive sensing technique [58–60]. After SCP calculations, the temperature-dependent anharmonic dynamical matrices are transformed into the real-space *effective* second-order IFCs at each temperature, which are then taken as inputs for subsequent *e-ph* coupling calculations.

The EPW code [52–54] is employed to calculate the *e-ph* matrix elements $g_{mnv}(\mathbf{k}, \mathbf{q})$. The required DFT calculations for the Wannier-Fourier interpolations are carried out within a uniform \mathbf{k} -point mesh of $8 \times 8 \times 8$. Then, to capture the accurate band gap, the GW quasiparticle corrections are imposed on energy eigenvalues $\varepsilon_{n\mathbf{k}}$ of states $|n\mathbf{k}\rangle$, while the wave functions maintain the DFT level. In EPW calculations, three Wannier functions above (below) the Fermi level are used to describe the conduction band (valence band), and the interpolated \mathbf{k} -point grid of $80 \times 80 \times 80$ and \mathbf{q} -grid of $40 \times 40 \times 40$ are applied to solve the precise $g_{mnv}(\mathbf{k}, \mathbf{q})$. From the $g_{mnv}(\mathbf{k}, \mathbf{q})$, the intrinsic electron mobility μ_e is computed by the linearized electronic BTE as [61,62]

$$\mu_{e,\alpha\beta} = \frac{-e}{n_e \Omega} \sum_{n \in \text{CB}} \int \frac{d\mathbf{k}}{\Omega_{\text{BZ}}} F_{n\mathbf{k},\alpha\beta}^0 \tau_{n\mathbf{k}} (1 + \Delta_{n\mathbf{k}}), \quad (2)$$

with $F_{n\mathbf{k},\alpha\beta}^0 \equiv v_{n\mathbf{k},\alpha} v_{n\mathbf{k},\beta} \partial f_{n\mathbf{k}}^0 / \partial \varepsilon_{n\mathbf{k}}$, where n_e denotes the electron doping concentration, Ω and Ω_{BZ} are the volume of the unit cell and first Brillouin zone (BZ), respectively, $v_{n\mathbf{k},\alpha} = \hbar^{-1} \partial \varepsilon_{n\mathbf{k}} / \partial k_\alpha$ is the electron group velocity, $f_{n\mathbf{k}}^0$ is the Fermi-Dirac distribution, and $\tau_{n\mathbf{k}} = 1 / (2\Sigma''_{n\mathbf{k}})$ is the electron relaxation time with $\Sigma''_{n\mathbf{k}}$ representing the imaginary part of Fan-Migdal self-energy [54]. $\Delta_{n\mathbf{k}}$ is a correction term that eliminates the inaccuracy of μ_e within the self-energy relaxation-time approximation (SERTA). If $\Delta_{n\mathbf{k}}$ is neglected, the SERTA result of μ_e is obtained, while inclusion of $\Delta_{n\mathbf{k}}$ refers to the so-called iterative BTE (IBTE) calculation of μ_e . Similarly, there is an expression of Eq. (2) for hole mobility μ_h . From μ and $\tau_{n\mathbf{k}}$, the electrical conductivity σ , thermopower S , and electron thermal conductivity κ_e are computed as [63]

$$\sigma_{\alpha\beta} = e(n_e \mu_{e,\alpha\beta} + n_h \mu_{h,\alpha\beta}), \quad (3)$$

$$S_{\alpha\beta} = -\frac{1}{eT} \frac{\sum_n \int \frac{d\mathbf{k}}{\Omega_{\text{BZ}}} (\varepsilon_{n\mathbf{k}} - \varepsilon_F) F_{n\mathbf{k},\alpha\beta}^0 \tau_{n\mathbf{k}}}{\sum_n \int \frac{d\mathbf{k}}{\Omega_{\text{BZ}}} F_{n\mathbf{k},\alpha\beta}^0 \tau_{n\mathbf{k}}}, \quad (4)$$

and

$$\kappa_{e,\alpha\beta} = -\frac{1}{\Omega T} \sum_n \int \frac{d\mathbf{k}}{\Omega_{\text{BZ}}} (\varepsilon_{n\mathbf{k}} - \varepsilon_F)^2 F_{n\mathbf{k},\alpha\beta}^0 \tau_{n\mathbf{k}} - T S_{\alpha\beta}^2 \sigma_{\alpha\beta}, \quad (5)$$

respectively, where ε_F denotes the Fermi level, and $\kappa_{e,\alpha\beta}$ is rational only when the SERTA result of σ is used.

III. RESULTS AND DISCUSSION

The atomic structure of the cubic Rb_3AuO is shown in Fig. 1(a). Our PBESOL optimization gives a lattice constant of 5.48 Å, which is slightly lower than the Perdew-Burke-Ernzerhof (PBE) functional result of 5.62 Å [39], but in good accordance with the experimental value of 5.50 Å [36,37,64].

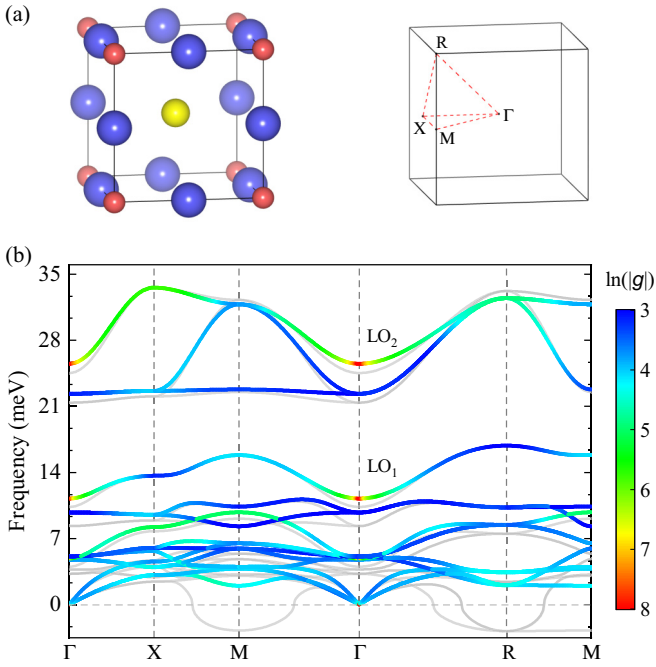


FIG. 1. (a) Atomic structure and BZ. The big blue, middle yellow, and small red balls label the Rb, Au, and O atoms, respectively. (b) Anharmonic phonon dispersion at 300 K with the projection of a ln-scale color map of the $|g_v(\mathbf{q})|$ in units of meV. The gray line represents the DFPT phonon dispersion.

The anharmonic phonon dispersion obtained from the *effective* second-order IFCs at 300 K is plotted in Fig. 1(b), in which the DFPT phonon dispersion is also shown for comparison. We observe that there is no imaginary frequency in the anharmonic phonon dispersion at 300 K, while the DFPT result exhibits the low-lying modes around the unstable M and R points. It has been demonstrated that the strong quartic anharmonicity of alkali-metal atoms plays a crucial role in anharmonic low-lying phonon frequency and structural stability of the cubic Rb_3AuO at finite temperature [34]. Meanwhile, the anharmonic low-lying modes harden evidently as the temperature increases, while the high-frequency modes have relatively weak anharmonic renormalization, as shown in Fig. 8. In fact, the eigenvalues of the *effective* second-order IFCs are always positive (even if the structure is unstable) by definition, as they describe the atomic fluctuations [65]. Therefore, to reveal a possible structural phase transition, the change of squared phonon frequencies with temperature for the softest low-lying mode is analyzed, which indicates that the cubic Rb_3AuO structure is stable at temperatures above 100 K [34].

To investigate the *e-ph* coupling strength on different phonon modes, a ln-scale color map of the quantities $|g_v(\mathbf{q})|$ at 300 K, which are obtained from the *e-ph* matrix elements $g_{mv}(\mathbf{k}, \mathbf{q})$ by integrating \mathbf{k} in the first BZ and computing the square root of the gauge-invariant trace of $|g|^2$ over three conduction bands, is overlaid on the anharmonic phonon dispersion at the same temperature. Here we focus on $|g_v(\mathbf{q})|$ induced by three conduction bands since the *n*-type case has superior electronic transport according to subsequent analysis. One can find that the two polar (longitudinal) optical branches

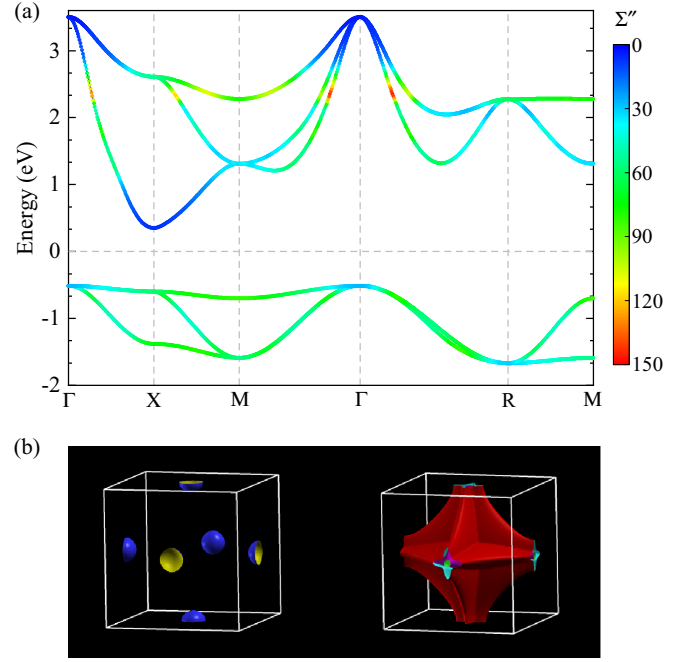


FIG. 2. (a) Quasiparticle band structure with the projection of a color map of the imaginary part of electron self-energy Σ''_{nk} (also known as the electron linewidth) in units of meV. (b) The isoenergy surface for the Fermi level ϵ_F dipped 100 meV into the conduction band (left) and valence band (right).

LO_1 and LO_2 , as labeled in Fig. 1(b), have fairly strong $|g_v(\mathbf{q})|$, especially around the BZ center, in sharp contrast to the projections of $|g_v(\mathbf{q})|$ on other phonon branches. In fact, the $|g_v(\mathbf{q})|$ values for the LO_1 and LO_2 modes diverge as $1/q$ for \mathbf{q} achieving the BZ center due to the Fröhlich interaction [66]. These findings signify that the *e-ph* coupling on the LO_1 and LO_2 branches dominates the electron scattering in the cubic Rb_3AuO . Furthermore, we can find that the anharmonic low-lying modes around the M and R points also possess certain *e-ph* coupling, which is usually deemed as zero when the DFPT phonons are used in solving Eq. (1) due to the presence of imaginary frequencies.

From DFT calculations within the GGA of the PBE (PBESOL) functional, a band gap of 0.24 (0.08) eV is obtained in the cubic Rb_3AuO . Since DFT usually underestimates the gap value, the GW quasiparticle calculation is carried out on top of the DFT wave functions with the GGA of the PBESOL functional selected in this work. The quasiparticle band structure is plotted in Fig. 2(a). We find that the cubic Rb_3AuO has an indirect gap of 0.86 eV with the conduction-band minimum (CBM) locating at the X point and the valence-band maximum (VBM) at the Γ point. The conspicuous characteristics are a dispersive conduction-band pocket around the CBM and a flat-and-dispersive valence-band pocket near the VBM, which generates a set of spheroidlike isoenergy surfaces around three X points at 100 meV above the CBM and an isoenergy surface composed of a large eight-vertex-concave shape surrounding an eight-vertex star and a small cube around the Γ point at 100 meV below the VBM, as shown in Fig. 2(b). The spheroidlike isoenergy surface reflects that the effective mass is small longitudinally (along the ΓX direction) and larger

but still small transversely (along the XM direction). The isoenergy surface at 100 meV below the VBM is actually formed by three valence bands (see Fig. 9), and illustrates the coexistence of small and large effective mass. Both kinds of band structures have been related to a high TE power factor.

The CBM pocket comes with threefold pocket multiplicity, which benefits σ by increasing the electron concentration for a given Fermi level ϵ_F and eliminates the adverse effect on S resulting from band misalignment [67]. Moreover, the small effective mass of the CBM pockets is supposed to contract the acoustic phonon-scattering phase space, a typical limitation of a carrier scattering process for TE materials. To verify this, we focus on the projections of the imaginary part of electron self-energy Σ''_{nk} (also known as the electron linewidth, an indicator of the e - ph coupling [53,68]) on the band structure to reveal intrinsic scattering at the CBM. As shown in Fig. 2(a), there exists a fairly small linewidth on the band around the CBM, which signifies a very weak e - ph scattering at the CBM. On the other hand, the fact that $|g_v(\mathbf{q})|$, dominated by three conduction bands, has a large strength on only polar optical branches illustrates the negligible coupling between electrons and acoustic phonons, interpreting the limitation of the acoustic phonon-scattering process and thus weak scattering at the CBM.

The renormalization of the real part of the electron self-energy can also influence the band structure. The renormalized quasiparticle band structures at 300, 500, and 800 K are shown in Fig. 10, which demonstrates that the dispersion trend near the CBM has negligible renormalization, consistent with the weak e - ph coupling around the CBM. In addition, the renormalization of the real part of the electron self-energy results in a slight decrease of the band gap, e.g., about 0.08 eV at 800 K, which has almost no effect on the final electronic and TE transport. These results signify that the renormalization of the real part of the electron self-energy for the band structure can be neglected in electronic transport calculations. Hence, unless otherwise stated, we take the GW quasiparticle band structure to study the electronic and TE properties in this work.

The SERTA and IBTE results of electron mobility μ_e and hole mobility μ_h are plotted in Fig. 3(a). Since the fusing point is about 850 K [37] and a latent structural phase transition has been predicted to occur at 100 K [34], we only show the mobility values between 100 and 800 K in Fig. 3(a). Overall, the μ_e is much higher than the μ_h , and the IBTE solutions from 100 to 800 K are about 55% to 61% (30% to 15%) larger than the SERTA results for electrons (holes). For instance, the μ_e obtained from the SERTA and IBTE calculations at 300 K are 285 and 454 cm^2/Vs , respectively, which is much higher than the corresponding results of about 9 and 11 cm^2/Vs for the μ_h at the same temperature. According to Eq. (2), the mobility is proportional to τ_{nk} and $|v_{nk}|^2$ if the SERTA calculation is performed in an isotropic crystal. For the cubic Rb_3AuO , the carrier scattering rates $1/\tau_{nk}$ around the VBM are more than three times larger than the scattering rates around the CBM, as shown in Fig. 4(a), and the magnitude of v_{nk} near the VBM is about one-third of that near the CBM, which finally causes the SERTA value of μ_e to be almost 30 times higher than that of μ_h , as shown in Fig. 3(a).

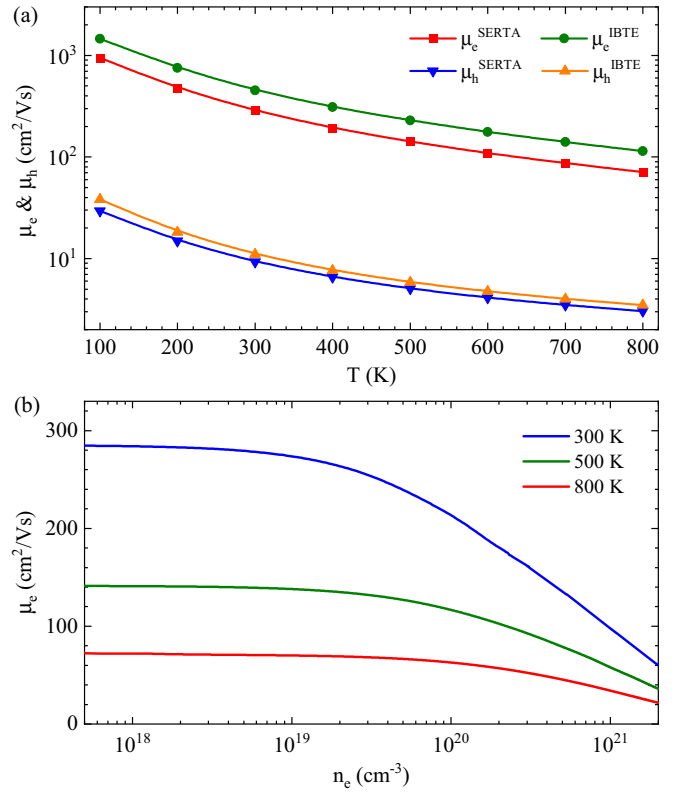


FIG. 3. (a) Calculated electron mobility μ_e and hole mobility μ_h as functions of temperature T . The results from the SERTA and IBTE calculations are both exhibited. (b) SERTA calculated electron mobility μ_e as functions of doping concentration n_e at 300, 500, and 800 K.

Another important point is the relatively weak temperature dependence of the calculated mobility. Generally, the enhancement of temperature leads to increasing phonon concentration, which gives rise to the enhanced carrier scattering rates, as shown in Fig. 4(a), and thus the lowered mobility, as shown in Fig. 3(a). Here we can approximately describe the temperature dependence of mobility μ in the cubic Rb_3AuO crystal by a power law $\mu \propto T^{-1.1}$ for both electrons and holes, which is weaker than the relation $\mu \propto T^{-\alpha}$ with $\alpha \sim 1.7$ – 2.4 for the μ in Si and Ge, but analogous to the power law $\mu_e \propto T^{-1.0}$ for the μ_e in GaAs [69]. Moreover, carrier concentration also plays an important role in mobility. As an example, the SERTA results of μ_e vs n_e at 300, 500, and 800 K are plotted in Fig. 3(b). One can find that μ_e decreases with n_e at a given temperature, and this decreasing is slight at low n_e , e.g., $< 10^{19}$ (10^{20}) cm^{-3} for the μ_e at 300 (800) K. Of course, at high n_e , the μ_e decreases drastically due to the enhanced scattering rates.

In addition, we also show the zoomed-in total and mode-resolved scattering rates $1/\tau_{nk}$ around the CBM at 300 K in Fig. 4(b). It can be clearly seen that the LO_1 and LO_2 optical modes dominate the total scattering rates, in line with the projections of mode-resolved e - ph coupling strength on the anharmonic phonon dispersion at 300 K in Fig. 1(b). Quantitatively, the scattering rates governed by the LO_1 and LO_2 phonons account for about 73% of the total scattering rates

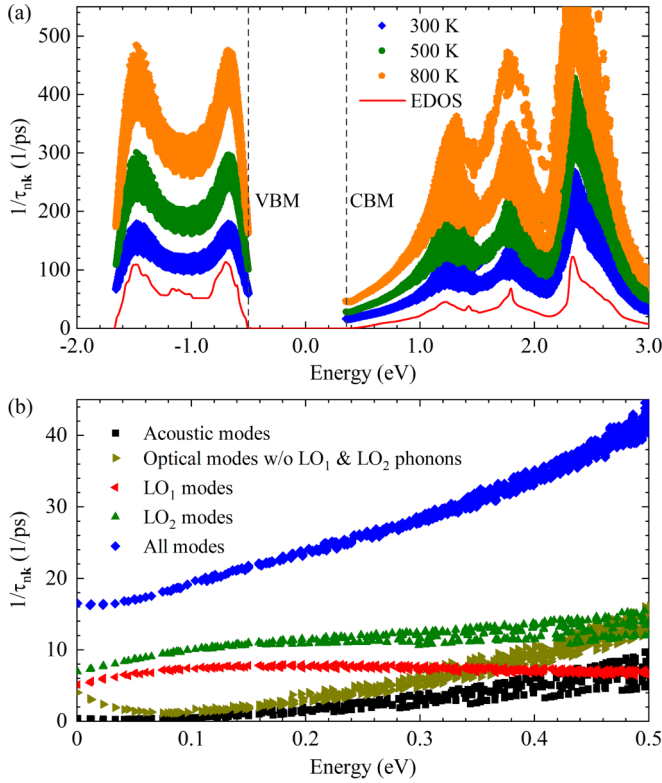


FIG. 4. (a) Total carrier scattering rates $1/\tau_{nk}$ at 300, 500, and 800 K. The red curve represents the electronic density of states (EDOS). Obviously, the scattering rates closely follow the EDOS. (b) Total and mode-resolved scattering rates $1/\tau_{nk}$ around the CBM at 300 K. The energy of the CBM is set to be zero.

at the CBM, while the optical phonons excluding LO_1 and LO_2 modes and all the acoustic phonons contribute about 25% and 3% of the total scattering rates, respectively, as shown in Fig. 4(b), which also demonstrates again the contraction of acoustic phonon scattering around the CBM.

We now turn to the TE behaviors. Due to the existence of high μ_e , we first concentrate on the n -type case to research the TE properties. The SERTA and IBTE results of electrical conductivity σ calculated from Eq. (3) at 300, 500, and 800 K are plotted in Fig. 5(a). For comparison, the σ at 300 and 800 K obtained from the Kubo-Greenwood electrical conductivity (KGEC) formulation [70] are also shown in Fig. 5(a). It can be found that the IBTE solution at 300 K is close to the KGEC value at the same temperature, while the σ of SERTA and IBTE at 800 K is much lower than the corresponding KGEC result. In view of the KGEC method excluding the e - ph scattering, the similarity of the IBTE solution at 300 K to the KGEC value exhibits the decoupled electron and phonon systems in the n -type case, which accords well with the weak e - ph scattering around the CBM and supports the high μ_e at low temperature. As temperature increases, the coupling between the electron and phonon systems strengthens, that is, the e - ph scattering is enhanced, and thus the σ at 800 K is much lowered relative to the KGEC result, as shown in Fig. 5(a). In addition, one can observe from Fig. 5(a) that the σ decreases with T at the same n_e , consistent with the change of μ_e vs T . However, because of the enhanced electronic

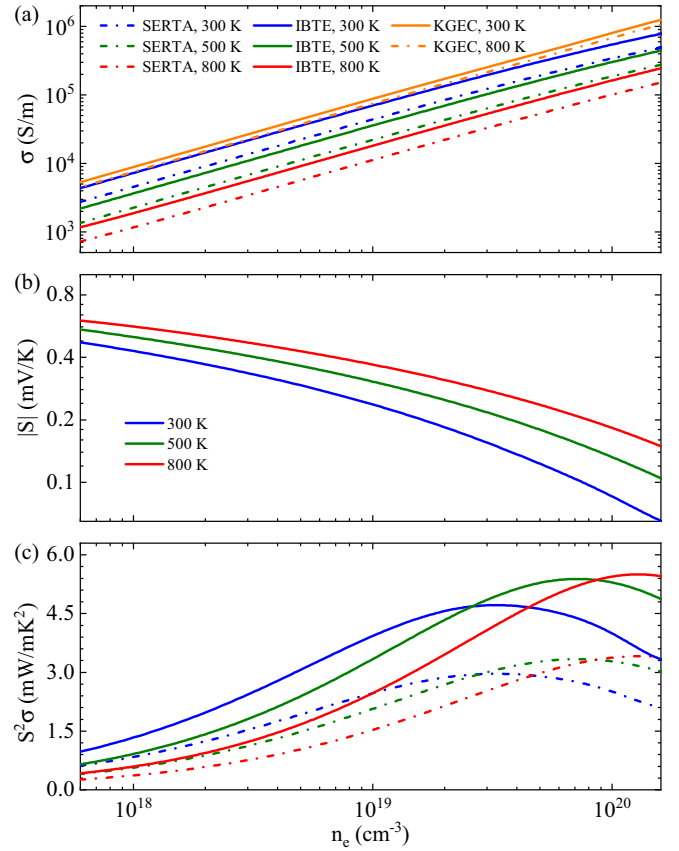


FIG. 5. TE parameters for the n -type cubic Rb_3AuO : (a) SERTA and IBTE results of electrical conductivity σ at 300, 500, and 800 K. The full and dashed orange lines denote the Kubo-Greenwood electrical conductivity (KGEC) at 300 and 800 K, respectively. (b) Thermopower $|S|$ at 300, 500, and 800 K. (c) Power factor $S^2\sigma$ calculated with the S in (b) and the SERTA and IBTE results of σ in (a). The curves have the same color legend as that in (a).

density of states (EDOS), the σ increases monotonously with increasing n_e at the same T , in spite of the decreasing μ_e shown in Fig. 3(b). Finally, it is worth noting that the IBTE electronic transport in many semiconductors is more pertinent than the SERTA result compared with the experimental value [61,62,71], which means that the TE performance computed with the IBTE solution of σ should also be taken as a reasonable reference.

The calculated thermopower S from Eq. (4) for the n -type cubic Rb_3AuO is shown in Fig. 5(b). Due to the minus value of S for the n -type case, the absolute value is plotted in Fig. 5(a) for convenience. As is expected, the calculated $|S|$ is fairly high due to the presence of threefold pocket multiplicity of the CBM. For instance, the $|S|$ at $n_e = 10^{19} cm^{-3}$ have values from 0.24 to 0.37 mV/K as T increases from 300 to 800 K, which are very high compared with the $|S|$ in the typical TE material PbTe [2], and consistent with the fact that the typical thermopower for a high- ZT material usually lies in the range of 0.2 to 0.3 mV/K. Moreover, one can note that the $|S|$ increases with T at the same n_e , and decreases with n_e at the same T , analogous to the general trend observed in most semiconducting TE materials. At last, because of the

coexistence of high $|S|$ and good charge transport, a very high TE power factor $S^2\sigma$ even reaching 5.4 (5.5) mW/mK² at 500 (800) K is obtained in the n -type cubic Rb₃AuO based on the IBTE solution of σ , as shown in Fig. 5(c). This is comparable to the highest n -type power factor of ~ 7 mW/mK² for bulk semiconductors reported to date [33]. At the same time, the $S^2\sigma$ with the SERTA result of σ is also exhibited in Fig. 5(c) for comparison, which gives a highest power factor of ~ 3.5 mW/mK², also considerably higher than that of commonly used TE materials.

Eventually, high ZT requires the coexistence of a high power factor and low thermal conductivity. The cubic Rb₃AuO has already been predicted to have low lattice thermal conductivity κ_l , e.g., ~ 0.7 W/mK at 300 K, using phononic BTE on top of the SCP calculations at each considered temperature with the input IFCs computed with the projector augmented wave potentials [72] in previous work [34]. For consistency and convenience, we reproduce the κ_l here based on the same method, but using the IFCs calculated with the norm-conserving potentials chosen in this paper. The reproduced result is shown in Fig. 6(a), which provides similar findings to previous calculations. As discussed in Ref. [34], the low κ_l derives mainly from the strong three-phonon scattering, and it has an anomalously weak temperature dependence of $\kappa_l \sim T^{-0.3}$ due to the presence of strong and different quartic anharmonic renormalization for the soft modes at different temperatures. Moreover, if other

effects such as thermal expansion and additional four-phonon scattering induced by the quartic anharmonicity are included, the κ_l may be further reduced and the temperature dependence may be somewhat different from the relation of $\kappa_l \sim T^{-0.3}$, which indicates a potential limitation of the present SCP + BTE method.

Because of low κ_l , electron thermal transport plays an important role in the ultimate TE performance. To calculate the electron thermal conductivity κ_e , the commonly used formula is described by Eq. (5), which corresponds logically to the σ obtained from the linearized electronic BTE within the relaxation-time approximation [63,73,74]. In other words, the formula of Eq. (5) is essentially a method within the relaxation-time approximation, and a reasonable Lorenz number L can be captured via the Wiedemann-Franz law $\kappa_e = L\sigma T$ based on this method with corresponding σ [33]. Obviously, combined with the obtained S and κ_l , the TE performance can be fully calculated from the σ and κ_e computed by this method. However, recent calculations show that the IBTE electronic transport in many semiconductors is higher and more pertinent than the SERTA result [61,62,71]. Therefore, to gain the TE properties within the IBTE and reveal the rational upper limit of the ZT value, the κ_e corresponding to the σ within the IBTE is required. Unfortunately, there is no numerically feasible formulation of the κ_e relating to the σ of IBTE to date. As a simple model, here we calculate the required κ_e from the σ of IBTE via the Wiedemann-Franz law $\kappa_e = L\sigma T$ with the reasonable Lorenz number L obtained from the σ and κ_e within the SERTA.

The calculated κ_e within the SERTA and IBTE for the n -type cubic Rb₃AuO are plotted in Fig. 6(b), in which the inset shows the obtained Lorenz number L scaled by the Wiedemann-Franz value $L_{WF} = (\pi^2/3)(k_B^2/e^2)$. Evidently, a similar trend to σ vs T and n_e is discovered for the κ_e in a wide range of the relevant doping concentration. Also, the κ_e of IBTE is higher than the SERTA result, which is meaningful to capturing a rational TE performance within the IBTE. Furthermore, one can observe a negative deviation of L from the Wiedemann-Franz value, that is, the L is much lower than the L_{WF} throughout the relevant doping ranges, e.g., $L/L_{WF} \sim 0.73$ – 0.62 at $n_e = 10^{19}$ cm⁻³ as T changes from 300 to 800 K. This small L is beneficial to gain the undersized κ_e , being indispensable for enhancement of ZT . The small L can be interpreted by a single parabolic band model, according to which L is written as $L = (r + 2.5)k_B^2/e^2$ [75], where the constant r is controlled by the energy dependence of e - ph scattering. Under polar optical phonon scattering, $r = 0.5$, which results in $L = 3k_B^2/e^2 < L_{WF}$. For acoustic phonon scattering, $r = -0.5$, and thus $L = 2k_B^2/e^2$ would be much lower than the L_{WF} . Last but not least, we can find that the κ_e within the IBTE is comparable to or even higher than the κ_l at lower temperature and higher doping concentration, e.g., $\kappa_e \sim 0.73$ W/mK at $T = 300$ K and $n_e = 2 \times 10^{19}$ cm⁻³.

The combination of high power factor and low thermal conductivity in the cubic Rb₃AuO gives rise to an anomalously high n -type $ZT \sim 3.31$ at $n_e \sim 1.6 \times 10^{19}$ cm⁻³ and $T = 800$ K based on the calculations with the IBTE electronic transport results, as shown by the full line in Fig. 7. This ZT value is much larger than those in most of the reported bulk TE materials, although somewhat lower than the highest $ZT \sim 5$

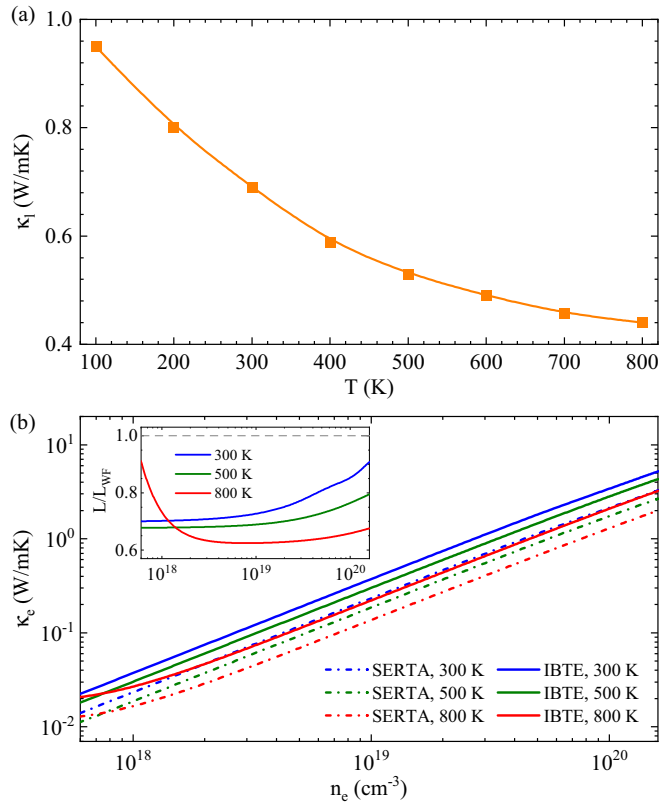


FIG. 6. (a) Lattice thermal conductivity κ_l . (b) SERTA and IBTE electron thermal conductivity κ_e at 300, 500, and 800 K. The inset exhibits the calculated Lorenz number L which is scaled by the Wiedemann-Franz value L_{WF} .

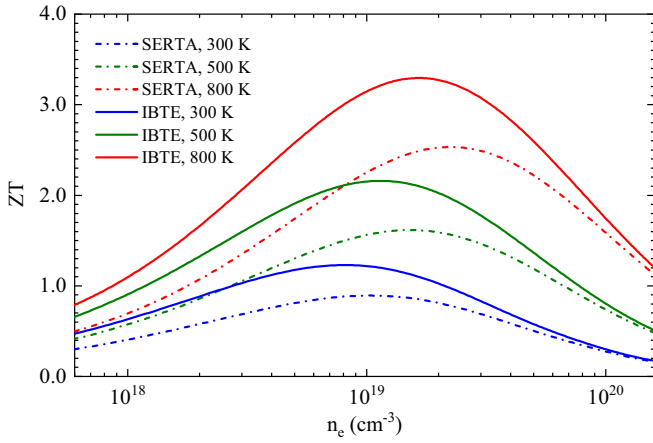


FIG. 7. Figure of merit ZT calculated with the SERTA and IBTE results of σ and κ_e for the n -type cubic Rb_3AuO at 300, 500, and 800 K.

predicted in the n -type Ba_2BiAu full-Heusler compound [33]. At the same time, at 300 K, we predict a $ZT \sim 1.23$ at $n_e \sim 8.1 \times 10^{18} \text{ cm}^{-3}$, which is also a very high value for the TE material at room temperature. Moreover, the doping concentrations $n_e \sim 8.1 \times 10^{18}$ and $1.6 \times 10^{19} \text{ cm}^{-3}$ correspond to the electron doping of about 0.0013 and 0.0026 e per unit cell, respectively, which can be easily accessible in experiments by weaker ionized-impurity scattering. For comparison, the ZT calculated from the SERTA results of σ and κ_e is also plotted, as shown by the dashed line in Fig. 7. We find that a maximum $ZT \sim 2.55$ is captured at $n_e \sim 2.3 \times 10^{19} \text{ cm}^{-3}$ and $T = 800 \text{ K}$ if the SERTA results of electronic transport are used. This value is also very high, and close to the highest experimental ZT result of 2.6 reported to date [11].

For testing the validity of our predictions for the TE properties, we also compute the n -type ZT using the BOLTZTRAP code [74] within the constant relaxation-time approximation. Since the algorithm implemented in the BOLTZTRAP code is analogous to Eqs. (2)–(5) but with $\Delta_{nk} = 0$ and $\tau_{nk} = \tau_0$ [74], the TE performances within the constant relaxation-time approximation should be similar to those within the SERTA if the required constant relaxation time τ_0 is set reasonably. To satisfy this, the τ_0 at each temperature is calculated from the scattering rates around the CBM shown in Fig. 4(a). Our result shows that a highest n -type $ZT \sim 2.66$ within the constant relaxation-time approximation is obtained at $n_e \sim 2.6 \times 10^{19} \text{ cm}^{-3}$ and $T = 800 \text{ K}$, as shown in Fig. 11, which is consistent with the maximum $ZT \sim 2.55$ within the SERTA.

Then we discuss the TE performance of the p -type case. Due to the presence of a flat-and-dispersive valence-band pocket around the VBM, the TE power factor $S^2\sigma$ of the p -type cubic Rb_3AuO is also considerably high, which derives from the combination of a drastically enhanced S and a much lowered μ_h with respect to those of the n -type case. As a result, the highest $ZT \sim 2.75$ (2.55) at $n_h \sim 4.7 \times 10^{20}$ (5.3×10^{20}) cm^{-3} and $T = 800 \text{ K}$ is obtained in the p -type cubic Rb_3AuO when the IBTE (SERTA) results of electronic transport are used. For details, see Fig. 12. However, compared with the n_e for the n -type case, the n_h here is about 30 to

60 times higher, meaning that achieving good TE properties in the p -type case is more difficult than that in the n -type one. Hence, the n -type cubic Rb_3AuO is recommended to realize the good TE performance in experiments.

We note that ionized impurity scattering is excluded in our present calculations. If this effect is taken into account, the calculated σ , κ_e , and thus ZT may be decreased somewhat. Since the CBM is fairly parabolic in the cubic Rb_3AuO , the Brooks-Herring formula can be used to estimate impurity scattering at the desired doping concentrations for the n -type case [76]. Based on the electron effective mass of $0.27m_e$ at the CBM in the isotropic approximation and the static permittivity of $14.2\epsilon_0$ for the cubic Rb_3AuO crystal (m_e and ϵ_0 are the mass of the free electron and vacuum permittivity, respectively), we estimate the electron mobility μ_{IMP} driven by ionized-impurity scattering through Eq. (36) in Ref. [76] to demonstrate the effect of ionized-impurity scattering on the final ZT , as shown in Fig. 13. Overall, the ionized-impurity scattering plays an important role in total electron mobility μ_{tot} at low temperature and high doping concentrations. As an example, at $n_e = 10^{19} \text{ cm}^{-3}$, the ionized-impurity scattering make the μ_{tot} decrease about 17% (25%), 10% (14%), and 5% (7%) at 300, 500, and 800 K, respectively, relative to the SERTA (IBTE) electron mobility μ_{e-ph} induced by only $e-ph$ scattering. Meanwhile, the corresponding σ and κ_e suffer from similar modification. As a result, the modified maximum n -type ZT is 3.15 at 800 K and 1.02 at 300 K, as shown in Fig. 13(b).

Thermal expansion is another factor that can influence the result of ZT , especially at high temperature. Due to the presence of imaginary frequency in the DFPT phonon dispersion, the commonly used quasiharmonic approximations are invalid to calculate thermal expansion here. As a rough estimation, we use the linear approximation to calculate the lattice constant at 800 K, in which the optimized value of 5.48 Å is taken as the lattice constant at zero temperature, that is, the effect of zero-point phonon energy on the lattice constant is neglected. From the experimental result of 5.50 Å at room temperature, we can obtain a constant thermal expansion coefficient of $\sim 3.66 \times 10^{-5} \text{ K}^{-1}$ and infer a lattice constant of 5.53 Å at 800 K. The thermal expansion coefficient here is analogous to the value of $\sim 2.98 \times 10^{-5} \text{ K}^{-1}$ for the similar cubic SrTiO_3 perovskite structure [77]. Using the lattice constant of 5.53 Å, our calculations indicate that the σ and κ_e for the n -type case at 800 K decrease about 16% while the κ_l reduce about 9%, which, as a result, makes the maximum n -type ZT be 3.16 at 800 K. If the ionized-impurity scattering and thermal expansion effect are both taken into consideration, the final maximum n -type ZT becomes 3.02 at 800 K, as shown in Fig. 14. In addition, the additional four-phonon scattering induced by the quartic anharmonicity may also play a role in the estimation of the lattice thermal transport and, consequently, the final ZT . Since the κ_l can be further reduced by the four-phonon scattering [78], the obtained ZT may increase somewhat if this effect is included in the estimation of the TE performance. Finally, for the p -type case, a high ZT approaching 2.4 can be captured at 800 K after the inclusion of thermal expansion and ionized-impurity scattering.

IV. CONCLUSION

In conclusion, we have systematically investigated the electronic transport and TE properties in the cubic Rb_3AuO crystal with strong lattice anharmonicity using first-principles calculations combined with SCP theory, e - ph coupling, and electronic BTE. Due to the failure of DFPT in solving e - ph matrix elements for a strongly anharmonic crystal, we have introduced the combination of SCP theory and Wannier-Fourier interpolation to calculate the e - ph coupling. We discovered a high electron mobility μ_e , e.g., $\sim 454 \text{ cm}^2/\text{Vs}$ at 300 K from the IBTE solution, in the n -type cubic Rb_3AuO , and demonstrated that the coupling between electrons and polar optical phonons dominate this good charge transport because the acoustic phonon-scattering phase space is contracted by small effective mass of the CBM pockets. At the same time, the light and threefold degenerate conduction-band pockets around the CBM give rise to a high thermopower S , which, along with the high μ_e , leads to a very high n -type power factor $S^2\sigma$, e.g., even reaching $5.5 \text{ mW}/\text{mK}^2$ at 800 K within the IBTE transport mechanism. Moreover, a low lattice thermal conductivity and an undersized Lorenz number that signifies a resulting low electron thermal conductivity were also found. As a result, a good TE performance with a figure of merit $ZT \sim 1.23$ at 300 K and an anomalously high $ZT \sim 3.31$ at 800 K was obtained in the n -type cubic Rb_3AuO , based on the calculations with IBTE results of the σ and κ_e driven by e - ph scattering. After the inclusion of ionized-impurity scattering in calculating the σ and κ_e of the IBTE, a modified n -type ZT is 1.02 at 300 K and 3.15 at 800 K. If the thermal expansion effect is also taken into account, the final maximum n -type ZT is further modified into 3.02 at 800 K. Therefore, considering the available experimental preparation scheme given by Feldmann, the cubic Rb_3AuO crystal may be the first bulk material for realizing TE conversion efficiency with $ZT > 3$. In addition, a $ZT \sim 2.4$ can also be found at 800 K in the p -type case, but at a much higher doping concentration compared with that in the n -type one. Hence, the n -type cubic Rb_3AuO is recommended to test the good TE performance in experiment.

ACKNOWLEDGMENTS

This research was supported by the National Natural Science Foundation of China under Grants No. 11704322, No. 11974302, No. 11774396, and No. 11774195; and the National Key Research and Development Program of China under Grants No. 2016YFA0300902 and No. 2016YFB0700102.

APPENDIX

1. SCP phonon dispersion at different temperature

The SCP phonon dispersion for the cubic Rr_3AuO at 300, 500, and 800 K is plotted in Fig. 8. The result is calculated through the real-space *effective* second-order IFCs that are transformed from the SCP calculated anharmonic dynamical matrices at each temperature. One can find that the low-frequency anharmonic modes, e.g., $\omega'_{qv} < 10 \text{ meV}$, harden with the increased temperature, while the high-frequency modes have a relatively small anharmonic renormalization.

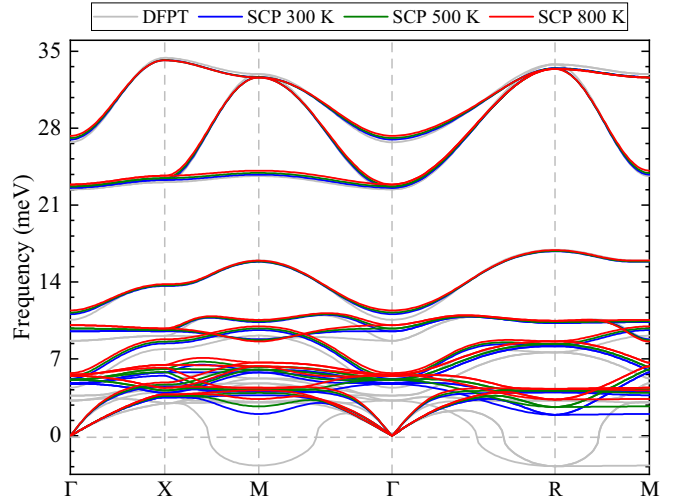


FIG. 8. Anharmonic phonon dispersion for the cubic Rr_3AuO at 300, 500, and 800 K. The DFPT phonon dispersion is also shown by the gray line for comparison.

2. Isoenergy surface around the VBM

As shown in Fig. 2(a), three valence bands contribute to the VBM simultaneously, and there is a flat-and-dispersive valence-band characteristic near the VBM, which, as a result, leads to a valence-band pocket with the isoenergy surface formed by a large eight-vertex-concave shape, as shown in Fig. 9(a), a middle eight-vertex star, as shown in Fig. 9(b), and a small cube, as shown in Fig. 9(c), at 100 meV below the VBM. This type of isoenergy surface supports the coexistence of small and large effective mass, and thus promises the presence of a high TE power factor.

3. Band structure renormalized by the real part of the electron self-energy

The quasiparticle band structures renormalized by the real part of the electron self-energy at 300, 500, and 800 K are plotted in Fig. 10. It shows that the dispersion around the CBM has negligible renormalization, in accordance with the weak e - ph coupling around the CBM. The negligible band renormalization near the CBM means a very weak change of the electron group velocity derived from the real part of the self-energy, and demonstrate that the unrenormalized quasiparticle band structure can be used to capture the electronic

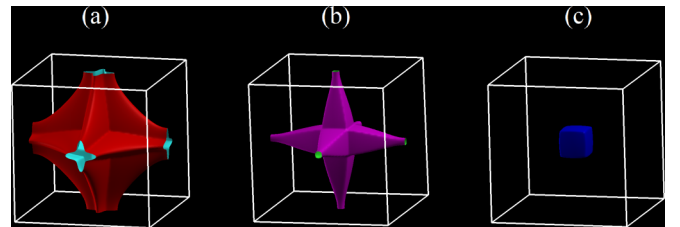


FIG. 9. The isoenergy surface for the Fermi level ϵ_F dipped 100 meV into the valence band. It is formed by (a) a large eight-vertex-concave shape surrounding (b) an eight-vertex star and (c) a small cube.

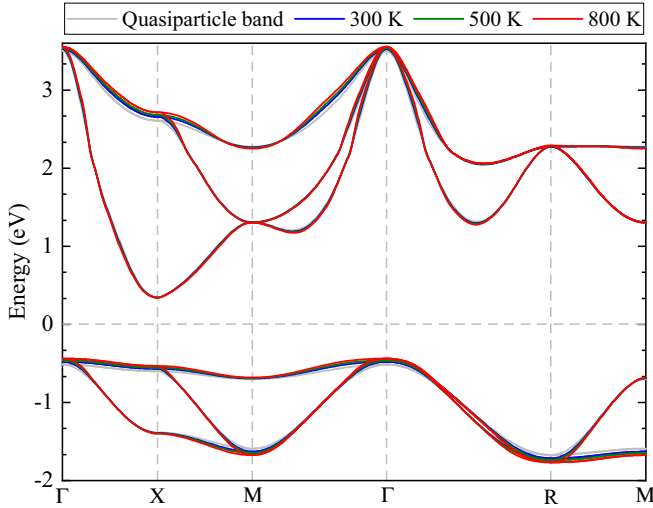


FIG. 10. Quasiparticle band structure renormalized by the real part of the electron self-energy at 300, 500, and 800 K. The unrenormalized quasiparticle band structure is plotted by the gray line for comparison.

transport properties with enough accuracy. In addition, the self-energy renormalization also leads to a slight decrease of the band gap, e.g., about 0.08 eV at 800 K, which also has a negligible effect on the final electronic transport performance.

4. TE results tested by BOLTZTRAP for the n -type cubic Rb_3AuO

The BOLTZTRAP code [74] within the constant relaxation-time approximation is employed to test the validity of our predictions for the TE properties. The n -type case is taken as an example. The required constant relaxation time τ_0 is calculated from the scattering rates around the CBM shown in Fig. 4(a). Due to weak scattering around the CBM, the calculated τ_0 at the CBM have considerably large values, such as 61.6, 35.7, and 21.5 fs at 300, 500, and 800 K, respectively, which are comparable to those around the CBM of Ba_2BiAu , as shown in Fig. 4(a) in Ref. [33]. Based on these values of τ_0 , a highest n -type $ZT \sim 2.66$ is obtained at $n_e \sim 2.6 \times 10^{19} \text{ cm}^{-3}$ and $T = 800 \text{ K}$, as shown in Fig. 11, which is consistent with the maximum $ZT \sim 2.55$ within the SERTA.

5. TE properties for the p -type cubic Rb_3AuO

The calculated thermopower S from Eq. (4) for the p -type cubic Rb_3AuO is shown in Fig. 12(a). Obviously, due to the presence of the flat band around the VBM, the calculated S is much higher than that in the n -type case. For instance, the S at $n_h = 10^{19} \text{ cm}^{-3}$ have values from 0.52 to 0.65 mV/K as T increases from 300 to 800 K, about two times those in the n -type case. However, because of the much reduced σ , the obtained power factor $S^2\sigma$ at $n_h = 10^{19} \text{ cm}^{-3}$ is about an order of magnitude lower than that at the same doping concentration in the n -type case, as shown in Fig. 5(c) and Fig. 12(b). Therefore, a high doping concentration is required to increase the σ and thus the $S^2\sigma$ for the p -type case. As shown in Fig. 12(b), a high $S^2\sigma$ achieving 3.9 mW/mK^2 at

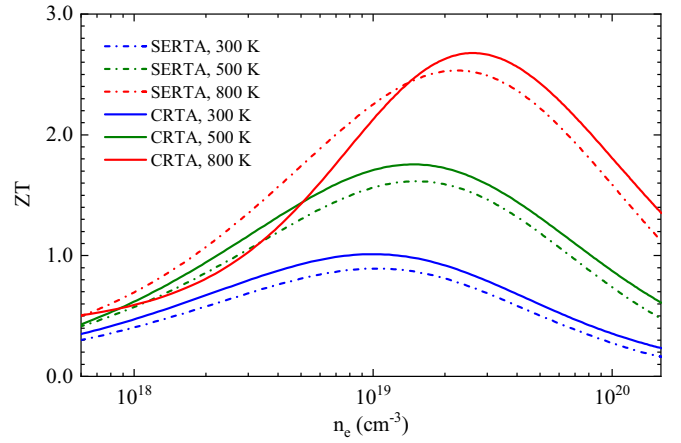


FIG. 11. Figure of merit ZT calculated within the relaxation-time approximation and the SERTA of σ , κ_e , and S for the n -type cubic Rb_3AuO at 300, 500, and 800 K.

$n_h \sim 1.7 \times 10^{21} \text{ cm}^{-3}$ and $T = 800 \text{ K}$ can be obtained in the p -type cubic Rb_3AuO if the IBTE solution of σ is applied in the calculation. Meanwhile, the $S^2\sigma$ calculated with the SERTA result of σ has the highest value of $\sim 3.4 \text{ mW/mK}^2$,

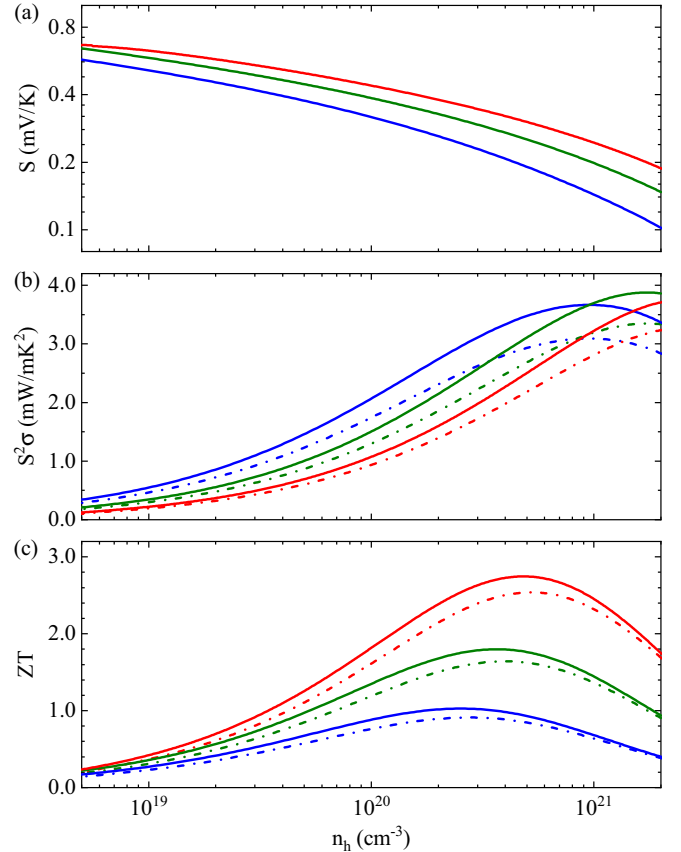


FIG. 12. TE parameters for the p -type cubic Rb_3AuO at 300, 500, and 800 K: (a) Thermopower $|S|$. (b) Power factor $S^2\sigma$ calculated with the SERTA and IBTE results of σ . (c) Figure of merit ZT calculated with the SERTA and IBTE results of σ and κ_e . The curves have the same color legends as that in Figs. 5 and 7.

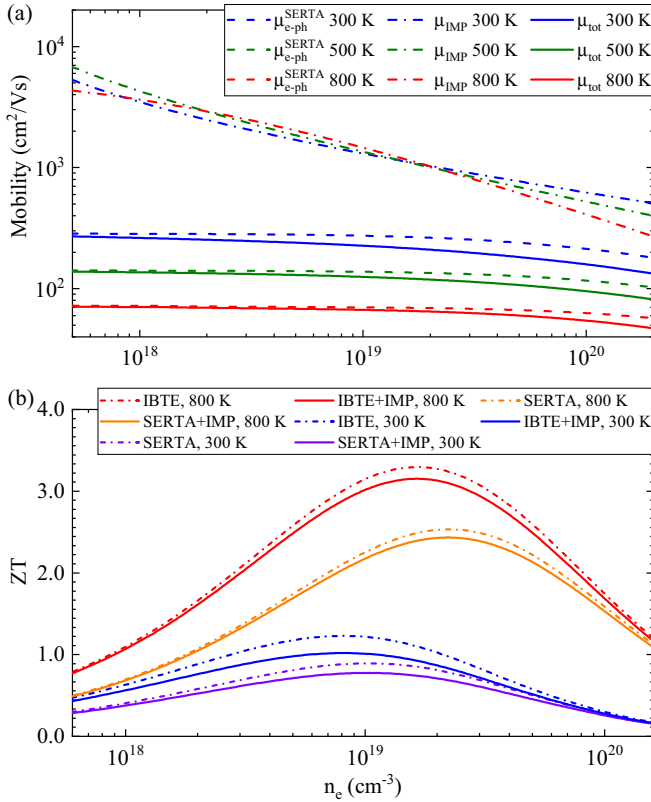


FIG. 13. (a) Electron mobility μ_{IMP} driven by ionized-impurity scattering, SERTA calculated mobility μ_{e-ph} driven by $e-ph$ scattering, and total mobility μ_{tot} with the contributions of $e-ph$ scattering and ionized-impurity scattering as functions of doping concentration n_e for the n -type case at 300, 500, and 800 K. (b) Figure of merit ZT calculated with the SERTA and IBTE results of σ and κ_e modified by the ionized-impurity scattering (IMP) for the n -type cubic Rb₃AuO at 300, 500, and 800 K.

which is also very high compared with that of commonly used TE materials. As a result, the highest $ZT \sim 2.75$ (2.55) at $n_h \sim 4.7 \times 10^{20}$ (5.3×10^{20}) cm⁻³ and $T = 800$ K is obtained in the p -type cubic Rb₃AuO based on the calculations with the IBTE (SERTA) solutions of σ and κ_e , as shown in Fig. 12(c).

6. Effect of ionized-impurity scattering on TE performance

The Brooks-Herring formula [79,80] is used to estimate ionized-impurity scattering for the n -type case. Using Eq. (36) in Ref. [76], the electron mobility μ_{IMP} driven by only the ionized-impurity scattering is estimated. The result, together with the SERTA electron mobility μ_{e-ph} and total mobility

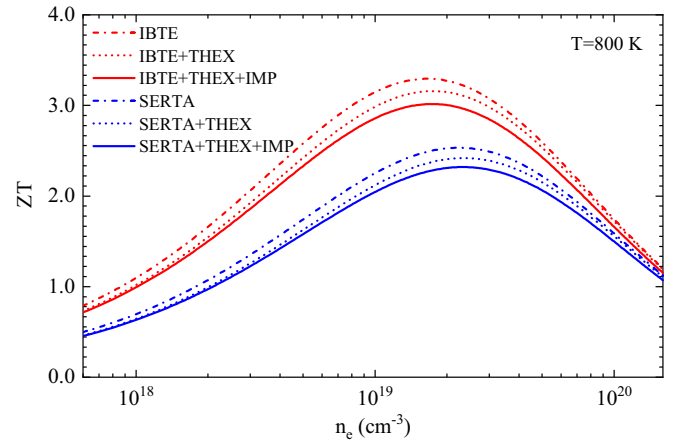


FIG. 14. Figure of merit ZT calculated with the SERTA and IBTE results of σ and κ_e without and with the inclusion of the thermal expansion (THEX) effect for the n -type cubic Rb₃AuO at 300, 500, and 800 K. The ZT result including both thermal expansion and ionized-impurity scattering (IMP) is also shown.

μ_{tot} , is plotted in Fig. 13(a). We find that the ionized-impurity scattering has considerable impact on the total electron mobility μ_{tot} at low temperature and high doping concentrations. For instance, the ionized-impurity scattering makes the μ_{tot} at $n_e = 10^{19}$ cm⁻³ reduce about 17%, 10%, and 5% at 300, 500, and 800 K, respectively, relative to the SERTA electron mobility μ_{e-ph} driven by only the $e-ph$ scattering, as shown in Fig. 13(a). If the IBTE calculated μ_{e-ph} is used, more decrease of the μ_{tot} will be induced by the ionized-impurity scattering, such as 25%, 14%, and 7% at 300, 500, and 800 K, respectively, at $n_e = 10^{19}$ cm⁻³. Meanwhile, the corresponding σ and κ_e undergo similar modification. As a result, the modified highest n -type ZT is 3.15 (2.44) at 800 K and 1.02 (0.78) at 300 K based on the IBTE (SERTA) calculations, as shown in Fig. 13(b).

7. Effect of thermal expansion on TE performance

Using the lattice constant of 5.53 Å at 800 K, the calculated σ and κ_e for the n -type case at 800 K decrease about 16%, and the κ_l reduce about 9%, relative to the results computed with the optimized lattice constant. As a result, the maximum n -type ZT within the IBTE (SERTA) becomes 3.16 (2.42) at 800 K. If thermal expansion and ionized-impurity scattering are both taken into account, the final maximum n -type ZT within the IBTE (SERTA) is 3.02 (2.32) at 800 K, as shown in Fig. 14.

[1] G. J. Snyder and E. S. Toberer, Complex thermoelectric materials, *Nat. Mater.* **7**, 105 (2008).
 [2] J. P. Heremans, V. Jovicic, E. S. Toberer, A. Saramat, K. Kurosaki, A. Charoenphakdee, S. Yamanaka, and G. J. Snyder, Enhancement of thermoelectric efficiency in PbTe by distortion of the electronic density of states, *Science* **321**, 554 (2008).

[3] J. R. Sootsman, D. Y. Chung, and M. G. Kanatzidis, New and old concepts in thermoelectric materials, *Angew. Chem., Int. Ed.* **48**, 8616 (2009).
 [4] M. Zebarjadi, K. Esfarjani, M. S. Dresselhaus, Z. F. Ren, and G. Chen, Perspectives on thermoelectrics: From fundamentals to device applications, *Energy Environ. Sci.* **5**, 5147 (2012).

- [5] H. J. Wu, L.-D. Zhao, F. S. Zheng, D. Wu, Y. L. Pei, X. Tong, M. G. Kanatzidis, and J. Q. He, Broad temperature plateau for thermoelectric figure of merit $ZT > 2$ in phase-separated $\text{PbTe}_{0.7}\text{S}_{0.3}$, *Nat. Commun.* **5**, 4515 (2014).
- [6] T. Tadano, Y. Gohda, and S. Tsuneyuki, Impact of Rattlers on Thermal Conductivity of a Thermoelectric Clathrate: A First-Principles Study, *Phys. Rev. Lett.* **114**, 095501 (2015).
- [7] G. S. Nolas, J. Poon, and M. Kanatzidis, Recent developments in bulk thermoelectric materials, *MRS Bull.* **31**, 199 (2006).
- [8] G. J. Snyder, M. Christensen, E. Nishikori, T. Caillat, and B. B. Iversen, Disordered zinc in Zn_4Sb_3 with phonon-glass and electron-crystal thermoelectric properties, *Nat. Mater.* **3**, 458 (2004).
- [9] L. Bjerg, B. B. Iversen, and G. K. H. Madsen, Modeling the thermal conductivities of the zinc antimonides ZnSb and Zn_4Sb_3 , *Phys. Rev. B* **89**, 024304 (2014).
- [10] X. Lu, D. T. Morelli, Y. Xia, F. Zhou, V. Ozolinš, H. Chi, X. Zhou, and C. Uher, High performance thermoelectricity in earth-abundant compounds based on natural mineral tetrahedrites, *Adv. Energy Mater.* **3**, 342 (2013).
- [11] L.-D. Zhao, S.-H. Lo, Y. Zhang, H. Sun, G. Tan, C. Uher, C. Wolverton, V. P. Dravid, and M. G. Kanatzidis, Ultralow thermal conductivity and high thermoelectric figure of merit in SnSe crystals, *Nature (London)* **508**, 373 (2014).
- [12] C. W. Li, J. Hong, A. F. May, D. Bansal, S. Chi, T. Hong, G. Ehlers, and O. Delaire, Orbitally driven giant phonon anharmonicity in SnSe , *Nat. Phys.* **11**, 1063 (2015).
- [13] W. Liu, X. Tan, K. Yin, H. Liu, X. Tang, J. Shi, Q. Zhang, and C. Uher, Convergence of Conduction Bands as a Means of Enhancing Thermoelectric Performance of n -Type $\text{Mg}_2\text{Si}_{1-x}\text{Sn}_x$ Solid Solutions, *Phys. Rev. Lett.* **108**, 166601 (2012).
- [14] Y. Pei, A. LaLonde, S. Iwanaga, and G. J. Snyder, High thermoelectric figure of merit in heavy hole dominated PbTe , *Energy Environ. Sci.* **4**, 2085 (2011).
- [15] Y. Zhang, J.-H. Bahk, J. Lee, C. S. Birkel, M. L. Snedaker, D. Liu, H. Zeng, M. Moskovits, A. Shakouri, and G. D. Stucky, Hot carrier filtering in solution processed heterostructures: A paradigm for improving thermoelectric efficiency, *Adv. Mater.* **26**, 2755 (2014).
- [16] X. Shi, J. Yang, J. R. Salvador, M. Chi, J. Y. Cho, H. Wang, S. Bai, J. Yang, W. Zhang, and L. Chen, Multiple-filled skutterudites: High thermoelectric figure of merit through separately optimizing electrical and thermal transports, *J. Am. Chem. Soc.* **133**, 7837 (2011).
- [17] D. G. Cahill, S. K. Watson, and R. O. Pohl, Lower limit to the thermal conductivity of disordered crystals, *Phys. Rev. B* **46**, 6131 (1992).
- [18] C. J. Vineis, A. Shakouri, A. Majumdar, and M. G. Kanatzidis, Nanostructured thermoelectrics: Big efficiency gains from small features, *Adv. Mater.* **22**, 3970 (2010).
- [19] D. T. Morelli, V. Jovicic, and J. P. Heremans, Intrinsically Minimal Thermal Conductivity in Cubic I-V-VI₂ Semiconductors, *Phys. Rev. Lett.* **101**, 035901 (2008).
- [20] M. D. Nielsen, V. Ozolinš, and J. P. Heremans, Lone pair electrons minimize lattice thermal conductivity, *Energy Environ. Sci.* **6**, 570 (2013).
- [21] A. J. Minnich, M. S. Dresselhaus, Z. F. Ren, and G. Chen, Bulk nanostructured thermoelectric materials: Current research and future prospects, *Energy Environ. Sci.* **2**, 466 (2009).
- [22] Sangyeop Lee, Keivan Esfarjani, Tengfei Luo, Jiawei Zhou, Zhiting Tian, and Gang Chen, Resonant bonding leads to low lattice thermal conductivity, *Nat. Commun.* **5**, 3525 (2014).
- [23] B. C. Sales, D. Mandrus, and R. K. Williams, Filled skutterudite antimonides: A new class of thermoelectric materials, *Science* **272**, 1325 (1996).
- [24] G. P. Meisner, D. T. Morelli, S. Hu, J. Yang, and C. Uher, Structure and Lattice Thermal Conductivity of Fractionally Filled Skutterudites: Solid Solutions of Fully Filled and Unfilled End Members, *Phys. Rev. Lett.* **80**, 3551 (1998).
- [25] J. L. Cohn, G. S. Nolas, V. Fessatidis, T. H. Metcalf, and G. A. Slack, Glasslike Heat Conduction in High-Mobility Crystalline Semiconductors, *Phys. Rev. Lett.* **82**, 779 (1999).
- [26] G. S. Nolas, J. L. Cohn, G. A. Slack, and S. B. Schujman, Semiconducting Ge clathrates: Promising candidates for thermoelectric applications, *Appl. Phys. Lett.* **73**, 178 (1998).
- [27] G. S. Nolas, G. A. Slack, D. T. Morelli, T. M. Tritt, and A. C. Ehrlich, The effect of rare-earth filling on the lattice thermal conductivity of skutterudites, *J. Appl. Phys.* **79**, 4002 (1996).
- [28] L. D. Hicks and M. S. Dresselhaus, Effect of quantum-well structures on the thermoelectric figure of merit, *Phys. Rev. B* **47**, 12727 (1993).
- [29] D. Parker, X. Chen, and D. J. Singh, High Three-Dimensional Thermoelectric Performance from Low-Dimensional Bands, *Phys. Rev. Lett.* **110**, 146601 (2013).
- [30] D. I. Bilc, G. Hautier, D. Waroquiers, G.-M. Rignanese, and P. Ghosez, Low-Dimensional Transport and Large Thermoelectric Power Factors in Bulk Semiconductors by Band Engineering of Highly Directional Electronic States, *Phys. Rev. Lett.* **114**, 136601 (2015).
- [31] K. F. Hsu, S. Loo, F. Guo, W. Chen, J. S. Dyck, C. Uher, T. Hogan, E. K. Polychroniadis, and M. G. Kanatzidis, Cubic $\text{AgPb}_m\text{SbTe}_{2+m}$: Bulk thermoelectric materials with high figure of merit, *Science* **303**, 818 (2004).
- [32] M. Hong, Z.-G. Chen, L. Yang, Y.-C. Zou, M. S. Dargusch, H. Wang, and J. Zou, Realizing zT of 2.3 in $\text{Ge}_{1-x-y}\text{Sb}_x\text{In}_y\text{Te}$ via reducing the phase-transition temperature and introducing resonant energy doping, *Adv. Mater.* **30**, 1705942 (2018).
- [33] J. Park, Y. Xia, and V. Ozolinš, High Thermoelectric Power Factor and Efficiency from a Highly Dispersive Band in Ba_2BiAu , *Phys. Rev. Appl.* **11**, 014058 (2019).
- [34] Y. Zhao, C. Lian, S. Zeng, Z. Dai, S. Meng, and J. Ni, Quartic anharmonicity and anomalous thermal conductivity in cubic antiperovskites A_3BO ($A=\text{K, Rb}$; $B=\text{Br, Au}$), *Phys. Rev. B* **101**, 184303 (2020).
- [35] C. Feldmann and M. Jansen, Gradual anionic character of gold in ternary perovskite type oxides, *J. Chem. Soc. Chem. Commun.* **9**, 1045 (1994).
- [36] C. Feldmann and M. Jansen, To the knowledge of new ternary oxides with anionic gold, *Z. Anorg. Allg. Chem.* **621**, 201 (1995).
- [37] M. Jansen, The chemistry of gold as an anion, *Chem. Soc. Rev.* **37**, 1826 (2008).
- [38] A. Pantelouris, G. Kueper, J. Hormes, C. Feldmann, and M. Jansen, Anionic gold in Cs_3AuO and Rb_3AuO established by x-ray absorption spectroscopy, *J. Am. Chem. Soc.* **117**, 11749 (1995).
- [39] A. Jain, S. P. Ong, G. Hautier, W. Chen, W. D. Richards, S. Dacek, S. Cholia, D. Gunter, D. Skinner, G. Ceder, and K. A.

- Persson, The Materials Project: A materials genome approach to accelerating materials innovation, *APL Mater.* **1**, 011002 (2013).
- [40] S. Baroni, S. de Gironcoli, A. Dal Corso, and P. Giannozzi, Phonons and related crystal properties from density-functional perturbation theory, *Rev. Mod. Phys.* **73**, 515 (2001).
- [41] C. Heil, S. Ponc e, H. Lambert, M. Schlipf, E. R. Margine, and F. Giustino, Origin of Superconductivity and Latent Charge Density Wave in NbS₂, *Phys. Rev. Lett.* **119**, 087003 (2017).
- [42] J.-J. Zhou, O. Hellman, and M. Bernardi, Electron-Phonon Scattering in the Presence of Soft Modes and Electron Mobility in SrTiO₃ Perovskite from First Principles, *Phys. Rev. Lett.* **121**, 226603 (2018).
- [43] N. R. Werthamer, Self-consistent phonon formulation of anharmonic lattice dynamics, *Phys. Rev. B* **1**, 572 (1970).
- [44] T. Tadano and S. Tsuneyuki, Self-consistent phonon calculations of lattice dynamical properties in cubic SrTiO₃ with first-principles anharmonic force constants, *Phys. Rev. B* **92**, 054301 (2015).
- [45] T. Tadano, Y. Gohda, and S. Tsuneyuki, Anharmonic force constants extracted from first-principles molecular dynamics: Applications to heat transfer simulations, *J. Phys.: Condens. Matter* **26**, 225402 (2014).
- [46] T. Tadano and S. Tsuneyuki, Quartic Anharmonicity of Rattlers and Its Effect on Lattice Thermal Conductivity of Clathrates from First Principles, *Phys. Rev. Lett.* **120**, 105901 (2018).
- [47] T. Tadano and S. Tsuneyuki, First-principles lattice dynamics method for strongly anharmonic crystals, *J. Phys. Soc. Jpn.* **87**, 041015 (2018).
- [48] Y. Oba, T. Tadano, R. Akashi, and S. Tsuneyuki, First-principles study of phonon anharmonicity and negative thermal expansion in ScF₃, *Phys. Rev. Mater.* **3**, 033601 (2019).
- [49] N. Marzari and D. Vanderbilt, Maximally localized generalized Wannier functions for composite energy bands, *Phys. Rev. B* **56**, 12847 (1997).
- [50] I. Souza, N. Marzari, and D. Vanderbilt, Maximally localized Wannier functions for entangled energy bands, *Phys. Rev. B* **65**, 035109 (2001).
- [51] A. A. Mostofi, J. R. Yates, Y.-S. Lee, I. Souza, D. Vanderbilt, and N. Marzari, WANNIER90: A tool for obtaining maximally-localised Wannier functions, *Comput. Phys. Commun.* **178**, 685 (2008).
- [52] F. Giustino, M. L. Cohen, and S. G. Louie, Electron-phonon interaction using Wannier functions, *Phys. Rev. B* **76**, 165108 (2007).
- [53] S. Ponc e, E. Margine, C. Verdi, and F. Giustino, EPW: Electron-phonon coupling, transport and superconducting properties using maximally localized Wannier functions, *Comput. Phys. Commun.* **209**, 116 (2016).
- [54] F. Giustino, Electron-phonon interactions from first principles, *Rev. Mod. Phys.* **89**, 015003 (2017).
- [55] J. P. Perdew, A. Ruzsinszky, G. I. Csonka, O. A. Vydrov, G. E. Scuseria, L. A. Constantin, X. Zhou, and K. Burke, Restoring the Density-Gradient Expansion for Exchange in Solids and Surfaces, *Phys. Rev. Lett.* **100**, 136406 (2008).
- [56] M. Van Setten, M. Giantomassi, E. Bousquet, M. Verstraete, D. Hamann, X. Gonze, and G.-M. Rignanese, The PseudoDojo: Training and grading a 85 element optimized norm-conserving pseudopotential table, *Comput. Phys. Commun.* **226**, 39 (2018).
- [57] P. Giannozzi, S. Baroni, N. Bonini, M. Calandra, R. Car, C. Cavazzoni, D. Ceresoli, G. L. Chiarotti, M. Cococcioni, I. Dabo *et al.*, QUANTUM ESPRESSO: A modular and open-source software project for quantum simulations of materials, *J. Phys.: Condens. Matter* **21**, 395502 (2009).
- [58] F. Zhou, W. Nielson, Y. Xia, and V. Ozoliņš, Lattice Anharmonicity and Thermal Conductivity from Compressive Sensing of First-Principles Calculations, *Phys. Rev. Lett.* **113**, 185501 (2014).
- [59] F. Zhou, W. Nielson, Y. Xia, and V. Ozoliņš, Compressive sensing lattice dynamics. I. General formalism, *Phys. Rev. B* **100**, 184308 (2019).
- [60] F. Zhou, B. Sadigh, D. Åberg, Y. Xia, and V. Ozoliņš, Compressive sensing lattice dynamics. II. Efficient phonon calculations and long-range interactions, *Phys. Rev. B* **100**, 184309 (2019).
- [61] S. Ponc e, D. Jena, and F. Giustino, Hole mobility of strained gan from first principles, *Phys. Rev. B* **100**, 085204 (2019).
- [62] S. Ponc e, E. R. Margine, and F. Giustino, Towards predictive many-body calculations of phonon-limited carrier mobilities in semiconductors, *Phys. Rev. B* **97**, 121201(R) (2018).
- [63] B. Liao, J. Zhou, B. Qiu, M. S. Dresselhaus, and G. Chen, Ab initio study of electron-phonon interaction in phosphorene, *Phys. Rev. B* **91**, 235419 (2015).
- [64] C. Feldmann and M. Jansen, To the crystal chemical similarity of auride and halide ions, *Z. Anorg. Allg. Chem.* **621**, 1907 (1995).
- [65] R. Bianco, I. Errea, L. Paulatto, M. Calandra, and F. Mauri, Second-order structural phase transitions, free energy curvature, and temperature-dependent anharmonic phonons in the self-consistent harmonic approximation: Theory and stochastic implementation, *Phys. Rev. B* **96**, 014111 (2017).
- [66] H. Fr ohlich, Electrons in lattice fields, *Adv. Phys.* **3**, 325 (1954).
- [67] Y. Pei, X. Shi, A. LaLonde, H. Wang, L. Chen, and G. J. Snyder, Convergence of electronic bands for high performance bulk thermoelectrics, *Nature (London)* **473**, 66 (2011).
- [68] Y. Zhao, Z. Dai, C. Zhang, C. Lian, S. Zeng, G. Li, S. Meng, and J. Ni, Intrinsic electronic transport and thermoelectric power factor in *n*-type doped monolayer MoS₂, *New J. Phys.* **20**, 043009 (2018).
- [69] D. R. Lide, *CRC Handbook of Chemistry and Physics*, Vol. 90 (CRC Press, Taylor and Francis, Boca Raton, FL, 2010).
- [70] L. Calderin, V. Karasiev, and S. Trickey, Kubo-Greenwood electrical conductivity formulation and implementation for projector augmented wave datasets, *Comput. Phys. Commun.* **221**, 118 (2017).
- [71] S. Ponc e, D. Jena, and F. Giustino, Route to High Hole Mobility in GaN Via Reversal of Crystal-Field Splitting, *Phys. Rev. Lett.* **123**, 096602 (2019).
- [72] G. Kresse and D. Joubert, From ultrasoft pseudopotentials to the projector augmented-wave method, *Phys. Rev. B* **59**, 1758 (1999).
- [73] Y. Zhao, Z. Dai, C. Lian, S. Zeng, G. Li, J. Ni, and S. Meng, Low lattice thermal conductivity and good thermoelectric performance of cinnabar, *Phys. Rev. Mater.* **1**, 065401 (2017).

- [74] G. K. Madsen and D. J. Singh, BoltzTraP. A code for calculating band-structure dependent quantities, *Comput. Phys. Commun.* **175**, 67 (2006).
- [75] G. S. Nolas, J. Sharp, and J. Goldsmid, *Thermoelectrics, Basic Principles and New Materials Developments*, Springer Series in Materials Science, Vol. 45 (Springer-Verlag, Berlin, Heidelberg, 2001), 1st ed.
- [76] D. Chattopadhyay and H. J. Queisser, Electron scattering by ionized impurities in semiconductors, *Rev. Mod. Phys.* **53**, 745 (1981).
- [77] D. de Ligny and P. Richet, High-temperature heat capacity and thermal expansion of SrTiO₃ and SrZrO₃ perovskites, *Phys. Rev. B* **53**, 3013 (1996).
- [78] Y. Xia, Revisiting lattice thermal transport in PbTe: The crucial role of quartic anharmonicity, *Appl. Phys. Lett.* **113**, 073901 (2018).
- [79] H. Brooks, *Advances in Electronics and Electron Physics*, Vol. 7 (Academic Press, New York, 1955), pp. 85–182.
- [80] P. P. Debye and E. M. Conwell, Electrical properties of *n*-type germanium, *Phys. Rev.* **93**, 693 (1954).